Phononic metagrating for lattice wave manipulation

Shuang Lu,[1] Zhongwei Zhang,[1] Yong Li,[1,*] Peter Hänggi,[2] and Jie Chen[1,†]
[1]*Center for Phononics and Thermal Energy Science, China–EU Joint Lab for Nanophononics, MOE Key Laboratory of Advanced Micro-structured Materials, School of Physics Science and Engineering, Tongji University, Shanghai 200092, People's Republic of China*
[2]*Institute of Physics, University of Augsburg, 86135 Augsburg, Germany*

(Received 26 September 2023; revised 16 December 2023; accepted 16 January 2024; published 5 February 2024)

The control of the phonon-wave behavior is of prominent interest for applications in thermal management and the processing of quantum information. In this work, we design and characterize a phonon-based grating nanostructure in a suspended single-layer graphene. The anomalous transmission of lattice waves and the controllable angle of the transmitted wave can be achieved via a skillful design of the underlying nanostructure and the mode conversion can be monitored *in situ*. An interesting nonlocal effect emerges due to the inherently strong covalent bondings. These features distinctly differ from former scenarios with acoustic waves. This work paves the way for the regulation of phonon transport by designing phonon-based metagrating structures.

DOI: 10.1103/PhysRevB.109.075404

I. INTRODUCTION

Wave manipulation using functional materials presents a salient objective in material physics. Back in 2011, a family of artificial materials emerged which display a generalization of Snell's law and were subsequently exploited for optical wave manipulation [1]. The burgeoning field of designing two-dimensional (2D) materials adds a new degree of freedom for various fascinating optical wave-front engineering capabilities [2–11], such as polarization control [2,3], light bending [4,5], anomalous transmission and reflection [12,13], and perfect absorption [6,7]. Inspired by these pioneering findings in optics, acoustic metamaterials [14–19] have also been developed to achieve interesting novel phenomena, such as acoustic bending [14], and asymmetric propagation [15]. These metamaterials thus enrich the amount of existing fundamental physical laws governing wave propagation.

The phonon exhibits both a wavelike and particle-like characteristics [20,21]. The particle-like characteristics have been well understood from the *incoherent* diffusive transport theory such as Boltzmann transport equations [22–24], and can be controlled by various scattering sources [25–28]. On the other hand, the importance of its wavelike nature, i.e., the *coherent* phonon aspect, has also been recognized over the past decade [29–34]. However, at the microscopic level, the complex and strong interaction between atoms might change the local control strategy of wave behaviors [35] and effective means to regulate the lattice wave are still lacking. Different from the optical and acoustic waves, phonons have the nature of wave-particle duality, so that the pure plane-wave form is not appliable but the phonon wave-packet picture, possessing a finite broadening, must be used instead. Moreover, in contrast to the acoustic waves, there are both transverse and longitudinal lattice waves in the crystal. The coupling mechanism between various phonon polarizations during the transmission of lattice waves through metagrating structure warrants further exploration.

Additionally, the wavelike nature allows for the control of wave information with multiple degrees of freedoms (DoFs) such as amplitude, phase, polarization, and wavelength. Regulating multiple or full DoFs of photons based on metamaterial has been used in optical encryption, which opens up a new door for high-security information storage and communications [36,37]. Similar efforts in developing information communication protocols utilizing the phase of phonons have recently been demonstrated [38]. In addition, introducing phonons as a bridge via the photon-phonon or microwave-phonon interaction provides feasible solutions for solid-state quantum chips by integrated photonic and superconducting quantum chips, which reveals the unique advantage for long-distance and low-loss transmission of quantum information [39]. In this process, the precise control and detection of individual phonons takes on a leading role for a coherent transfer of quantum states between superconducting qubits [40,41]. As such, the effective control of lattice waves is of significant importance.

We next demonstrate the control for both phase and transmission direction of lattice waves in a suspended single-layer graphene. The propagation of lattice waves is found to obey the generalized Snell law, as detailed with Eq. (1) below. Being distinctly different from a single-polarization excitation in the acoustic system, here both transverse acoustic (TA) and longitudinal acoustic (LA) phonons can be excited in the crystal due to the mode conversion between them. In contrast to the situation in acoustics where discrete and decoupled functional units are often used, our study utilizes the continuous and *atomic-scale* design of the functional elements so that they are inherently coupled to each other through their interatomic interactions. This in turn ensures an advantage for a robust design of the structural parameters.

*Corresponding author: yongli@tongji.edu.cn
†Corresponding author: jie@tongji.edu.cn

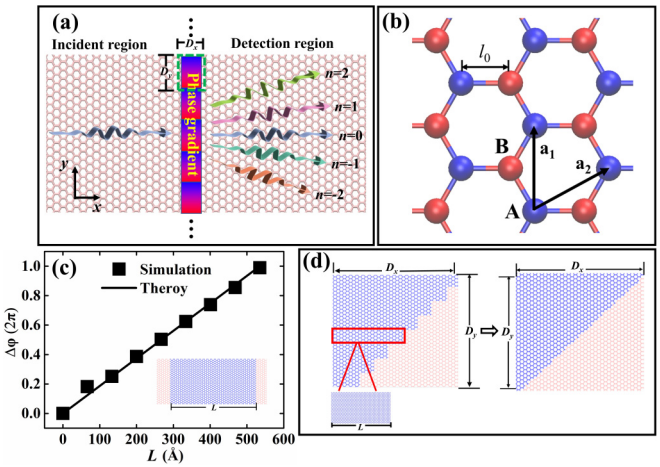

FIG. 1. (a) Schematic design of the phononic grating structure embedded in a single-layer graphene. A normal incident lattice wave ($k_y^0 = 0$) is scattered into different diffraction orders after passing through the grating structure. The grating structure has a thickness of D_x, and a period length of D_y along the y direction. (b) Lattice structure of graphene in the real space. $\mathbf{a_1}$ and $\mathbf{a_2}$ are the primitive-cell vectors, while A (blue) and B (red) represent two atoms ($j = 1$ and $j = 2$) in the primitive cell. The C–C bond length is denoted as l_0. (c) Phase changes of lattice waves passing through ^{14}C layers with different lengths L. The inset shows the atomic structure in one segment, where the blue (red) atom represents ^{14}C (^{12}C) atom. (d) Schematic of the functional unit for phase control. Top panel shows the discrete design by vertically stacking eight ^{14}C layers with different lengths together, while the bottom panel shows the continuous design via a triangular ^{14}C layer. All simulations in this work are carried out based on the continuous design.

This work is organized as follows: In Sec. II, we introduce the phonon metagrating system and present our simulation scheme. The main results are discussed in Sec. III. We verify the accuracy of simulation methods in Sec. III A. The deflection of the transmitted wave is analyzed in both real space and reciprocal k space in Sec. III B. The mode-conversion phenomenon and an intriguing nonlocal effect are discussed in Secs. III C and III D, respectively. The generalized Snell law has been validated in Sec. III E. Finally, a summary and the discussion are presented in Sec. IV.

II. THEORY AND SIMULATION METHODS

A. The generalized Snell law and phonon metagrating design

Specifically, let us consider an incident lattice wave along the x direction, as shown with Fig. 1(a). Our proposed metagrating nanostructure is composed of a series of periodically arranged functional units (cf. the single dashed box with the size of $D_x \times D_y$) along the y direction. In order to build up the phase gradient along the y direction, each functional unit should achieve a phase control from 0 to 2π. The phase gradient satisfies $\xi = \frac{d\varphi}{dy} = \frac{2\pi}{D_y} = G$, where G denotes the inverse lattice vector. This implies that the presence of a phase gradient will alter the wave vector by ξ in the y direction, causing the normal incidence mode to exhibit an anomalous transmission behavior. The periodicity of the metagrating structure along the y direction gives rise to a set of discrete modes $G_m = mG$, where m is an integer. Both the phase gradient and periodicity of the metagraring govern the lattice wave transmission at the interface according to the generalized Snell law as [1]

$$k_0(\sin\theta_t - \sin\theta_i) = \xi + G_m = (m+1)G = G_n, \quad (1)$$

where k_0 is amplitude of the incident wave vector, $\theta_t(\theta_i)$ denotes the transmitted (incident) angle, and $n = m + 1$ is the index for the transmitted lattice wave. Figure 1(a) displays a schematic example for the normal incident case ($k_y^0 = 0$). In a special case with *no* interactions between the functional units, i.e., with a local design (see detailed discussion in Sec. III D), the periodicity term G_m can be neglected, leading to the dominance of deflection mode $n = 1$ due to the phase gradient.

For a given polarization, the generalized Snell law implies the conservation of phonon wave-vector amplitude for different diffraction modes, i.e., $k_x^2 + k_y^2 = k_0^2$ for in-plane modes. Meanwhile, the elastic process at low temperature requires the conversion of the phonon energy after diffraction (at the same frequency). In crystals, the phonon wave vector and frequency are coupled via the phonon dispersion relation. To simultaneously ensure the conservation of both phonon wave vector and its frequency, this requires that the equal-frequency surface of the system is circular with respective to the wave vector. This condition can be satisfied in graphene, because graphene is an isotropic material and the difference in the wave-vector amplitude between different phonons with the same frequency is extremely small in the long-wavelength limit. Consequently, we consider the propagation of the long-wavelength acoustic (both TA and LA) phonons in the metagrating structure.

Since the phonon group velocity is material dependent, the phase gradient can be realized by use of different materials. For simplicity, we take a suspended single-layer graphene [lattice structure shown in Fig. 1(b)] as an example, and use the carbon isotopes (^{12}C and ^{14}C) to build up the phase gradient. Compared to the pure ^{12}C graphene, the phase change of the lattice wave after passing through a rectangular ^{14}C graphene layer with length L [cf. inset in Fig. 1(c)] can be calculated as follows:

$$\Delta\varphi = \frac{(v_1 - v_2)}{v_2}\frac{2\pi L}{\lambda}, \quad (2)$$

where $v_1(v_2)$ denotes the phonon group velocity in ^{12}C (^{14}C) graphene, and λ denotes the phonon wavelength.

In our simulation, we calculate the phase change by detecting the relative positions of the phonon wave packet (see Sec. II B). Figure 1(c) depicts both, the calculation results (solid line) according to Eq. (2) and simulation results (squares) for the phase difference in eight individual ^{14}C layers with different L, where an excellent agreement is observed. Having confirmed the feasibility and accuracy of individual phase control, we vertically stack eight ^{14}C layers with different lengths to cover the phase shift of 2π span, as shown in the left panel of Fig. 1(d). Such a discrete design of the functional unit can further be simplified to a triangle ^{14}C layer, as shown in the right panel of Fig. 1(d). All simulations in this work are carried out based on the continuous design.

B. The phonon wave-packet method

We use the wave-packet simulation method to monitor the phonon transmission process in a realistic structure. Periodic boundary conditions are adopted in both x- and y directions. A Gausian phonon wave packet at wave vector $\mathbf{k}$ and branch index s with a spatial width η in coordinate space can be described as [42,43]

$$u_{jl\alpha}(t) = A\varepsilon_{js\alpha} e^{i\mathbf{k}\cdot(\mathbf{R}_l-\mathbf{R}_0)} e^{-(\mathbf{R}_l-\mathbf{R}_0)^2/\eta^2} e^{-i\omega t}, \tag{3}$$

where $u_{il\alpha}(t)$ represents the α component of displacement at time t for atom j in the lth primitive cell. A denotes the amplitude of the wave packet, ω is the phonon frequency, and $\varepsilon_{js\alpha}$ is the phonon eigenvector for atom j. As shown in Fig. 1(b), there are two atoms ($j = 1$ and $j = 2$) in the primitive cell of the graphene lattice. The parameter η is used to control the spatial width of the Gaussian phonon wave packet, which is inversely proportional to the width of the phonon distribution function in the reciprocal space. Once $\mathbf{k}$ is specified, $\varepsilon_{js\alpha}$ and ω are determined from the phonon-dispersion relation by diagonalizing the dynamical matrix.

The initial set of atom velocities can be computed from the time derivative of the atomic displacement as $v_{il\alpha}(t) = \partial u_{il\alpha}(t)/\partial t$. All the structures have been optimized at 0 K. All our wave-packet simulations in this work are performed by using the LAMMPS package [44] with the optimized Tersoff potential [45]. Here, the C–C bond length is set as $l_0 = 1.44$ Å, and the lattice constant $a = \sqrt{3}l_0$ and $q_0 = \frac{2\pi}{l_0}$ for convenience. In our simulations, the amplitude A is set as $A = 0.001a = 0.0025$ Å and the parameter η is set as $\eta = 50a = 124.70$ Å. The time step is set as 0.5 fs.

It is worth mentioning that semianalytical techniques have been widely used to study the wave propagation process in electromagnetic and optical systems [46,47]. The hard boundary condition is often used in continuum theory for these systems. In the atomic system, however, the local environment at the interface (e.g., the atomic structure and interaction) is quite different from the bulk, giving rise to the unique interfacial phonon modes which are absent in the bulk spectrum [48]. These interfacial modes exist within a few layers adjacent to the interface, suggesting that a thin region should be considered as the "interface," rather than a planelike atomic sharp interface. Within this interfacial region, various conversions and redistributions of phonon modes will occur. These effects unfortunately cannot be captured by the continuum theory, but can be modeled accurately by the atomic-level numerical simulations.

In addition, acoustic and optical systems adopt the plane-wave solution for the incident wave, which is an ideally coherent wave without broadening in the reciprocal k space. In this case, the reflected and transmitted waves also maintain the characteristics of plane waves. Consequently, this enables the derivation of the wave evolution in these systems by using the continuum theory. For the lattice wave, however, due to the wave-particle duality of phonons, the phonon wave-packet picture with finite broadening must be used instead of a pure plane-wave form. When the incident wave is a Gaussian wave packet, the reflected and transmitted waves become very complex and no longer retain a Gaussian waveform. These above-mentioned challenges make it difficult to derive the evolution of lattice wave passing through the metagrating based on semianalytical techniques, which might be an intriguing problem deserving of future explorations.

C. Two-dimensional fast Fourier transform analysis

The 2D fast Fourier transform (FFT) of the atomic displacement is implemented via the following auxiliary definition:

$$B_{j\alpha}(\mathbf{k}) = \sum_l u_{jl\alpha} e^{-i\mathbf{k}\cdot\mathbf{R}_l}, \tag{4}$$

where $u_{jl\alpha}$ represents the α component of the displacement for atom j in the lth primitive cell, while $\mathbf{k}$ and $\mathbf{R}_l$ denote, respectively, the wave vector and the position of the lth primitive cell. The inverse Fourier transform can be described as

$$u_{jl\alpha} = \frac{1}{N}\sum_{\mathbf{k}} B_{j\alpha}(\mathbf{k}) e^{i\mathbf{k}\cdot\mathbf{R}_l}, \tag{5}$$

where N is the atom number, and the inverse Fourier transform for the nth-order component can be described as

$$u_{jl\alpha}(\mathbf{k}_n) = \frac{1}{N} B_{j\alpha}(\mathbf{k}_n) e^{i\mathbf{k}_n\cdot\mathbf{R}_l}, \tag{6}$$

where the $\mathbf{k}_n$ represents the wave vector of the nth-order diffraction mode. Therefore, both $B_{j\alpha}(\mathbf{k})$ and $u_{jl\alpha}(\mathbf{k}_n)$ have the dimension of the length.

III. RESULTS AND DISCUSSION

A. The verification of 2D FFT and wave-packet simulation

To verify the accuracy of the 2D FFT analysis and the wave-packet simulation, we first consider the propagation of a TA wave packet (propagation along the x direction with displacement along the y direction) in a pure graphene sheet without metagrating structure. The initial wave vector is set as $k_0 = \frac{2\pi}{\lambda} = 0.0373$ ($2\pi/$Å), and we let the TA wave packet evolve for a long time and then compute the 2D FFT of the atomic displacement. The top panel of Fig. 2(a) shows the 2D FFT of the atomic displacement in the y direction (u_y) for atom $j = 1$ in the primitive cell, which reveals the computed wave vector is 0.0375 ± 0.001 ($2\pi/$Å), in good agreement with our initial setting.

The bottom panel of Fig. 2(a) shows the 2D FFT of the atomic displacement in the x direction (u_x) for the same atom, and no mode appears. Since the displacement in the x direction corresponds to a LA mode, the absence of a phonon mode in the bottom panel of Fig. 2(a) indeed verifies the orthogonality between LA and TA modes, which futher highlights the accuracy of our FFT analysis and simulation methods. Moreover, Fig. 2(b) further shows the corresponding FFT results for atom $j = 2$ in the primitive cell, and the same results are obtained. Therefore, the choice of atom j does not affect the major feature in the FFT analysis. This conclusion also holds for the metagrating structure and has been confirmed in Appendix A.

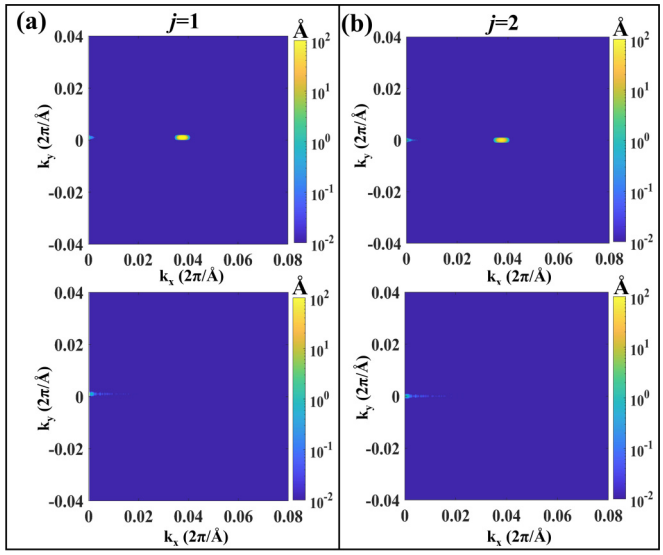

FIG. 2. The 2D FFT of different atoms (a) $j = 1$ and (b) $j = 2$ in the primitive cell for propagation of lattice wave that evolves a long time in pure suspended single-layer graphene. The top and bottom panel show the 2D FFT of the atomic displacement u_y and u_x, respectively. The side-bar color codings represent the amplitude of the FFT results $B_{j\alpha}(\mathbf{k})$ for the transmitted modes in the unit of Å. Here, the TA mode with $k_0 = 0.0373$ $(2\pi/\text{Å})$ is used as the normally incident wave packet.

B. Wave characteristics

After achieving the phase gradient (see Sec. II A), we launch the lattice wave packet on the left side, and monitor the transmitted wave on the right side. To focus on the physical mechanism, we consider the normal incidence in this work; i.e., $k_y^0 = 0$. Here, we use the TA mode with $\lambda = 26.8$ Å as the incident wave packet for demonstration, which corresponds to an initial wave vector $k_0 = 2\pi/\lambda = 0.0373$ $(2\pi/\text{Å})$. Similar phenomena have also been observed for other polarization modes. First, the ^{14}C triangular structure with $D_y = 124.6$ Å and $D_x = 550$ Å is adopted in our simulations. We find in our simulations that the reflected wave only accounts for 2% of the total incident energy, due to the relatively small impedance mismatch between the metagrating and pure graphene. Therefore, we focus only on the transmitted wave in our study, emphasizing the governing mechanism for the transmitted wave characteristics.

After the lattice wave passes through the triangle structure, the distribution of the atomic displacement in the y direction (u_y) is depicted with Fig. 3(a). The waveform of the transmitted wave is quite different from the original Gaussian wave packet, thus proving that the phononic grating structure affects the propagation of the lattice wave. However, it is difficult to directly probe the wave characteristics of the transmitted lattice wave in real space because different orders of diffraction modes become mixed.

In order to extract the wave characteristics at an individual mode level, a 2D FFT of the atomic displacement is performed; for details of the FFT and inverse FFT analysis see Sec. II C. The left panel of Fig. 3(b) depicts the FFT analysis on u_y. For a normal incident case, this polarization corresponds to the TA mode. Here, the color coding represents the amplitude of the FFT results. As indicated with the dashed line box in the left panel of Fig. 3(b), nine distinct modes with different k_y values are observed, which correspond to the zeroth, ±1st, ±2nd, ±3rd, and ±4th-order diffractive modes (± signs correspond to the $\pm y$ direction). For the 0th order, the calculated wave vector is $k_y = 0$ and $k_x = 0.0375 \pm 0.001$ $(2\pi/\text{Å})$; this agrees well with our initial wave vector, $k_0 = 0.0373$ $(2\pi/\text{Å})$. The origin for these discrete modes is due to the fact that k_x is real valued only when $k_0^2 > (k_0 \sin\theta_i + G_n)^2$. This requirement demands that the set of k_y values only assumes a finite number of propagation modes. The total number and the direction of those propagating modes are controlled by the phonon wavelength λ and the structure period D_y.

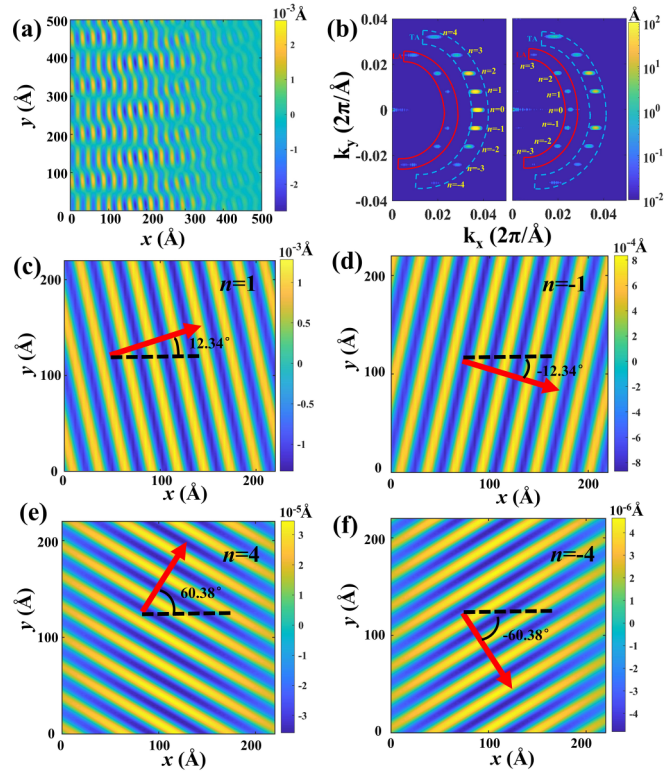

FIG. 3. (a) The distribution of the atomic displacement u_y for the transmitted wave in real space. Here, $D_y = 124.6$ Å and $D_x = 550$ Å are used in the simulations. (b) The 2D FFT of the atomic displacement u_y (left panel) and u_x (right panel) in the reciprocal space. The dashed (solid) line box represents the TA (LA) mode. Notice there exists weak $n = -3$ LA mode and $n = -4$ TA mode. (c)–(f) The inverse 2D FFT for different diffraction orders in real space. The arrow points to the propagation direction, and the angle denotes the diffraction angle. The side-bar color codings in (a) and (c)–(f) represent the displacement amplitude in real space, while that in (b) represents the amplitude of the FFT results in the reciprocal space. All color codings carry a dimension of length.

To visualize the field distributions of these discrete modes, the inverse 2D FFT was performed on the ±1st and ±4th modes, as depicted in Figs. 3(c)–3(f). A clear wave pattern is observed for each mode. More importantly, our simulation results agree excellently with the predictions based on the generalized Snell law in Eq. (1). For instance, for $n = 1$ mode in Fig. 3(c), the measured angle between the propagation

direction (pointed by the arrow) and the x axis is 12.34°, which is also consistent with arctan $\frac{k_y}{k_x} = 12.34°$. When plugging the corresponding parameters ($\lambda = 26.8$ Å and $D_y = 124.6$ Å) into Eq. (1), the generalized Snell law predicts a diffraction angle at 12.43° for $n = 1$ mode, which perfectly agrees with our measured result from the wave-packet simulation.

C. Mode conversion

Interestingly, also some unexpected modes with a different wave vector k_x emerge in the FFT analysis on u_y; note the solid line box in the left panel of Fig. 3(b). These extra modes have the same k_y as the expected modes in the dashed line box, but their intensity is much weaker. This is so because for modes with an arbitrary polarization, the value k_y is only determined by the period width in the y direction. A similar situation is observed alike in the FFT analysis on the atomic displacement in the x direction (u_x), as shown in the right panel in Fig. 3(b). Moreover, we have verified that our calculation results for different wave vectors in Fig. 3(b) satisfy the relation $k_x^2 + k_y^2 = k_0^2$, showing a circular shape as indicated by the solid- and dashed line boxes in Fig. 3(b). We find the radius of the circle $k_0 = 0.0375$ ($2\pi/$Å) for various modes in the dashed line box, while $k_0^{'} = 0.0255$ ($2\pi/$Å) for those modes in the solid line box.

This finding is in clear contrast from a situation using acoustic systems in air [1,49,50]. Only longitudinal polarization exists for the acoustic wave propagating in air or in a liquid, because shear forces do not exist in gases and liquids, while lattice waves propagating in solids exhibit both longitudinal and transverse modes. Considering this difference between the lattice wave and acoustic wave, we speculate that the mode conversion occurring between the TA and LA modes in our setup triggers this emergence of those additional modes in our FFT analysis.

To examine this feature, we depict in Fig. 4(a) the low-frequency part of phonon-dispersion relation of graphene calculated via lattice dynamics at 0 K. Near the Γ point, there are two in-plane branches (LA and TA) with linear dispersion, and an out-of-plane flexural acoustic (ZA) branch with quadratic dispersion. At low temperature, the elastic phonon scattering dominates, i.e., the same phonon frequency after the mode conversion. For the initially launched TA wave packet with $k_0 = 0.0373$ ($2\pi/$Å), the elastic scattering gives rise to a LA mode with a smaller wave vector $k_0^{'} = 0.0260$ ($2\pi/$Å), as indicated by the two dashed lines in Fig. 4(a), due to the larger group velocity of the LA branch. Interestingly, k_0 and $k_0^{'}$ marked in the phonon dispersion in Fig. 4(a) correspond perfectly to the calculated wave-vector amplitude in the dashed- and solid line box in Fig. 3(b), respectively. This agreement indeed confirms our hypothesis that the occurrence of those additional modes in fact originates from the mode conversion between LA and TA phonons. It further also explains the absence of the 0th order of LA (TA) in the left (right) panel of Fig. 3(b), originating from the orthogonality between LA and TA polarizations.

Previous studies on one-dimensional superlattices found that mode conversion does occur only for oblique incident lattice waves [51,52]. This is because the mode conversion

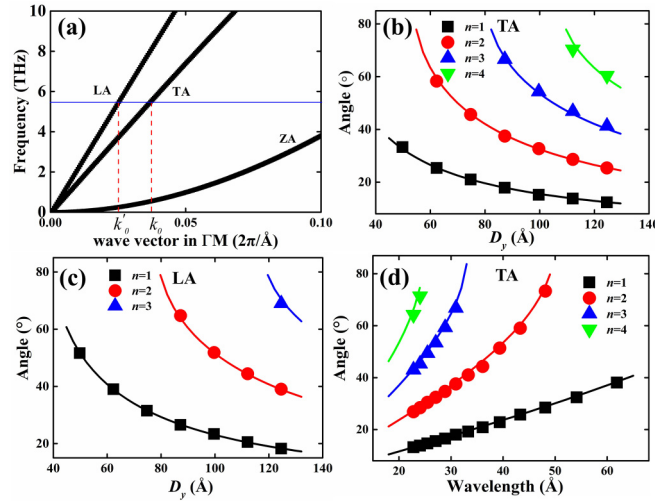

FIG. 4. (a) The phonon dispersion of graphene at low frequency in ΓM direction from the lattice dynamics calculation. k_0 represents the wave-vector amplitude of the initially launched TA mode along x direction, and $k_0^{'}$ denotes the wave-vector amplitude of the corresponding LA mode with the same frequency. The solid horizontal line is plotted as a guide to the eye. The low-lying curve represents the ZA branch with quadratic dispersion. (b) and (c) show the dependence of transmission angle on the structure period D_y for TA and LA modes, respectively. (d) The transmission angle vs. wavelength of the TA mode for a fixed $D_y = 99.7$ Å. The solid lines in (b) and (c) represent the calculation results of Eq. (1), while the symbols denote the simulation results.

is absent if the direction of polarization and the orientation of the interface remain the same. Although we launch a normal incident lattice wave onto the phononic grating structure, there exists an inclined interface *inside* this grating structure [cf. Fig. 1(a)]; this in turn allows for the detected mode conversion taking place.

D. Nonlocal effect

According to the generalized Snell law in Eq. (1), the direction of the transmitted lattice wave is governed simultaneously by the phase gradient ξ and the periodicity term G_m. In the *nonlocal* design considering the interactions between the functional units, the periodicity term G_m also plays an important role, and the nonlocal effect manifests itself by redistributing the energy among different diffraction orders ($n = m + 1$). This feature can be witnessed in Fig. 3(b), where multiple diffraction modes emerge. Another notable feature in Fig. 3(b) is the different FFT amplitudes occurring between positive and negative order modes, i.e., the asymmetric transmission between the positively and negatively deflected modes. This is because our phononic metagrating breaks the space symmetry and causes the lattice wave to propagate preferably in the direction of the decreasing phase gradient [53,54]. In addition to this asymmetry, the transmitted modes emerge in a wide range of deflection angles, decreasing in amplitude with larger deflection angles.

Our results are in distinct contrast from the case of using an acoustic setup. In acoustics, each phase control unit is separately designed while the role of the interaction among them is

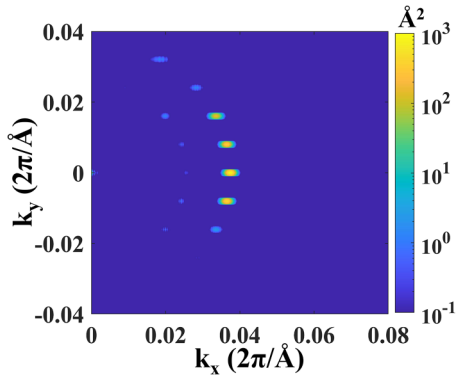

FIG. 5. The energy distribution of transmitted lattice wave. The side-bar color coding represents the amplitude of mode energy in the unit of Å^2. Here, $D_y = 124.6$ Å and $D_x = 550$ Å are used in the simulations, and the TA mode with $k_0 = 0.0373$ $(2\pi/\text{Å})$ is used as the normally incident wave packet.

neglected [14,50]. Consequently, such a *local* design strategy excludes the energy exchange among the phase-control units, so that the transmitted energy typically concentrates on a particular deflection angle. For instance, Estakhri *et al.* [55] reported that the normally incident acoustic wave prefers to propagate along +1st order after passing through the acoustic metasurface. They found the transmitted acoustic wave concentrates on the $n = 1$ order with nearly 100% of the incident energy under a small deflection angle. Similar phenomenon has also been observed in optical systems [1]. In contrast, the phase-control units in our system are inherently connected by the covalent bonds as shown in Fig. 1(d). This results in a strong nonlocal coupling among different phase control units and consequently causes an energy exchange among them. In fact, this nonlocal effect causes a redistribution of energy among different diffraction modes.

In order to quantitatively show the influence of nonlocal effect, we calculate the energy distribution of each diffraction mode. The energy of the nth diffraction mode $E(\mathbf{k}_n)$ depends on the squared modulus of the amplitude and the vibration frequency. The vibration frequency of diffraction modes remains the same due to the energy conservation law. The mode energy $E(\mathbf{k}_n)$ is proportional to the amplitude as

$$E(\mathbf{k}_n) \propto \sum_{j\alpha} |B_{j\alpha}(\mathbf{k}_n)|^2. \tag{7}$$

Figure 5 shows the mode energy distribution for an incident TA wave packet with $k_0 = 0.0373$ $(2\pi/\text{Å})$ passing through the metagrating with $D_y = 124.6$ Å and $D_x = 550$ Å. The energy ratio between the +1st order and −1st order in our study is only 1.34:1, and the +1st order mode accounts for less than 30% of the total energy, being much smaller than those observed in acoustics [55]. This nonlocal effect therefore constitutes a unique feature of our phononic metagrating system.

Interestingly, this intrinsic nonlocal effect can greatly simplify the structure design; particularly, a design rule of the 2π phase span is no longer necessary. Instead, the characteristic transmitted modes are mainly controlled by the structure period. To this end, we vary the horizontal structure length D_x while keeping the vertical structure period D_y fixed. We find that the length D_x has a negligible impact on the transmission angle (see Fig. 7 in Appendix B). Besides, the notable reduction of the horizontal structural thickness barely affects the distribution of diffraction modes. The small thickness clearly favors the maintenance of coherence for the propagating lattice wave, which presents a prerequisite for phonon interference effects.

E. Validation of the generalized Snell law

According to Eq. (1), the angle of the transmitted wave is related to the wavelength λ and the structure period D_y. In order to verify the generality of our setup, we next simulate the transmission process of the lattice wave propagation under different simulation parameters. Because the angles of positive and negative orders are symmetric [cf. Fig. 3(b)], we only depict the angle dependence on D_y for the positive orders with TA and LA polarizations in Figs. 4(b) and 4(c), respectively. Our simulation results (symbols) agree with the theoretical predictions (solid lines) by Eq. (1) for both polarizations. The corresponding 2D FFT results of the transmitted wave are shown in Fig. 8 in Appendix C. In addition, to examine the wavelength dependence we also launch the TA wave packet with different wavelengths and a fixed structure period ($D_y =$ 99.7 Å) to examine the wavelength dependence. As shown in Fig. 4(d), an excellent agreement between our simulation results and theory is obtained.

Although our study is demonstrated in a two-dimensional system, the realization in three-dimensional systems is also possible upon using a more complex design. In addition to the isotopes, the phase-control unit can further be realized by the combination of different materials with existing nanofabrication techniques [29,56–58]. Moreover, the experimental techniques for the excitation [59,60] and modulation [61,62] of coherent phonons are presently also available. For instance, previous works have demonstrated that utilizing light-plasmons coupling with the help of electrically generated surface acoustic waves is an effective way to excite the graphene plasmons with the required wave vector [63,64]. Besides, the generation and control of phonon wave packets on a single graphene nanoribbon using broadband laser pulses have been successfully demonstrated in experiment [65].

IV. CONCLUSION

In conclusion, we examined a powerful regulation scheme for lattice wave propagation upon skillfully devising an atomic metagrating struture being embedded in a suspended single-layer graphene. Its operation has been verified via detailed phonon wave-packet simulations. The resulting diffraction patterns found in our simulation depend on the period width D_y and the phonon wavelength λ, and agree excellently with the predictions by the generalized Snell law in Eq. (1). Distinct from the case of conventional acoustic systems, the mode conversion between TA and LA polarizations can be monitored directly. Due to the continuous phase regulation and the strong interatomic interaction, a remarkable nonlocal coupling effect emerges with our scheme. Further, the nonlocal effect makes the transmission angle only depend on the structure period D_y, while the remaining structural

parameters do affect the energy distribution of the diffraction modes. This in turn facilitates the maintenance of the phonon coherence with a small thickness of the metagrating structure. Our findings thereby evidence the feasibility for regulating lattice wave transmission via a suitable implementation of this metagrating design of atomic structures. Being so, the present study proves beneficial for various applications such as achieving the controllable heat transport across mesoscopic phononic devices, or alike also for suitable applications emerging in the area of quantum computing scenarios.

ACKNOWLEDGMENTS

This project is supported in part by the grants from the National Natural Science Foundation of China (Grants No. 12075168 and No. 11890703), the Science and Technology Commission of Shanghai Municipality (Grant No. 21JC1405600), and the Fundamental Research Funds for the Central Universities (Grant No. 22120230212).

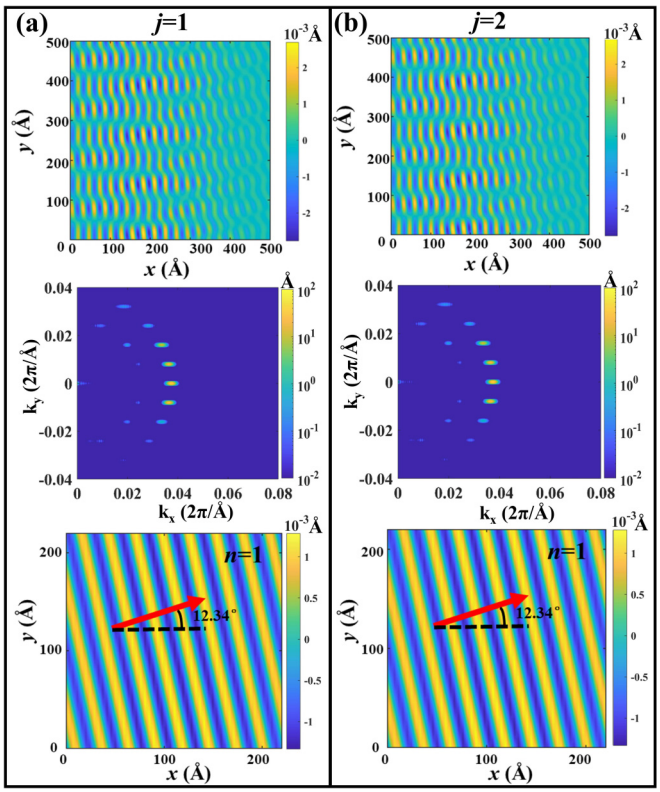

FIG. 6. The effect of different atoms (a) $j = 1$ and (b) $j = 2$ in the primitive cell for the propagation of lattice wave in the suspended single-layer graphene with the metagrating structure. The top, middle, and bottom panels show, respectively, the spatial distribution of u_y, the corresponding 2D FFT, and the inverse 2D FFT of the $n = 1$ mode. The side-bar color codings of the top and bottom panels represent the amplitude of transmitted modes in real space. The color codings for the middle panel represent the amplitude of the FFT results $B_{j\alpha}(\mathbf{k})$ for the transmitted modes. All the color codings have the length dimension. Here, $D_y = 124.6$ Å and $D_x = 550$ Å are used in the simulations, and the TA mode with $k_0 = 0.0373$ $(2\pi/\text{Å})$ is used as the normally incident wave packet.

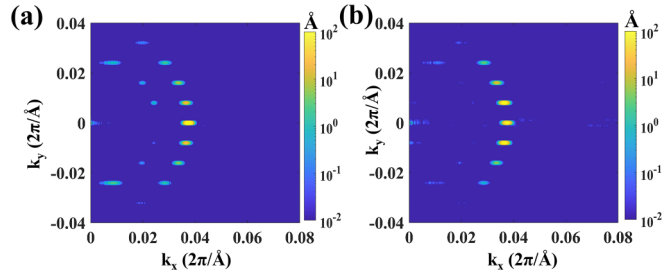

FIG. 7. The 2D FFT of u_y after the phonon wave passes through the metagrating structure with (a) $D_x = 200$ Å and (b) $D_x = 700$ Å. The side-bar color coding represents the amplitude of the FFT results $B_{j\alpha}(\mathbf{k})$ for the different transmitted modes in the unit of Å. The angle and number of transmission modes remain the same, showing only minor variations in the intensity, as shown with the side bar. Here, $D_y = 124.6$ Å is used in the simulations, and the TA mode with $k_0 = 0.0373$ $(2\pi/\text{Å})$ is used as the normally incident wave packet.

APPENDIX A: THE EFFECT OF ATOM CHOICE ON 2D FFT IN METAGRATING STRUCTURE

We initially launch a normal incident TA wave packet with $k_0 = 0.0373$ $(2\pi/\text{Å})$ in a suspended single-layer graphene with the metagrating structure ($D_y = 124.6$ Å and $D_x = 550$ Å), and record the atomic displacement distribution after passing through the metagrating structure. Figure 6 compares the distribution of u_y, the corresponding 2D FFT, and the inverse 2D FFT ($n = 1$ order) for different atoms ($j = 1$ and $j = 2$) in the primitive cell. We find that the calculation results for different atoms remain *qualitatively* the same, depicting only minor differences caused by the absolute value of the phonon eigenvectors $\varepsilon_{js\alpha}$ in Eq. (3) for different atoms. Therefore, we choose $j = 1$ throughout our study to discuss the underlying physical mechanisms in the metagrating structure.

APPENDIX B: EFFECT OF METAGRATING STRUCTURE THICKNESS D_x ON THE TRANSMITTED LATTICE WAVE

In order to verify the conclusion that the nonlocal effect can greatly simplify the structure design, we vary length D_x while keeping the vertical structure period D_y fixed. As shown in Figs. 7(a) and 7(b), the angle and number of transmission modes remain the same for $D_x = 200$ Å and $D_x = 700$ Å. The change of length D_x only affects the distribution of energy in different modes.

APPENDIX C: THE 2D FFT RESULTS FOR METAGRATING STRUCTURE WITH DIFFERENT WIDTHS

In order to verify the accuracy of our analysis and validate the generalized Snell law, a set of six additional period widths are adopted and the corresponding 2D FFT of the transmitted wave is used to analyze the resulting mode information. As shown in Fig. 8, with increasing the period width, the number of modes in the transmitted wave also increases and the number of transmitted modes is fully consistent with the prediction by Eq. (1). Similar to Fig. 3(b), the transition between TA and LA modes also occurs in all structures. The deflection angles of different polarized phonon modes are shown in Figs. 4(b) and 4(c).

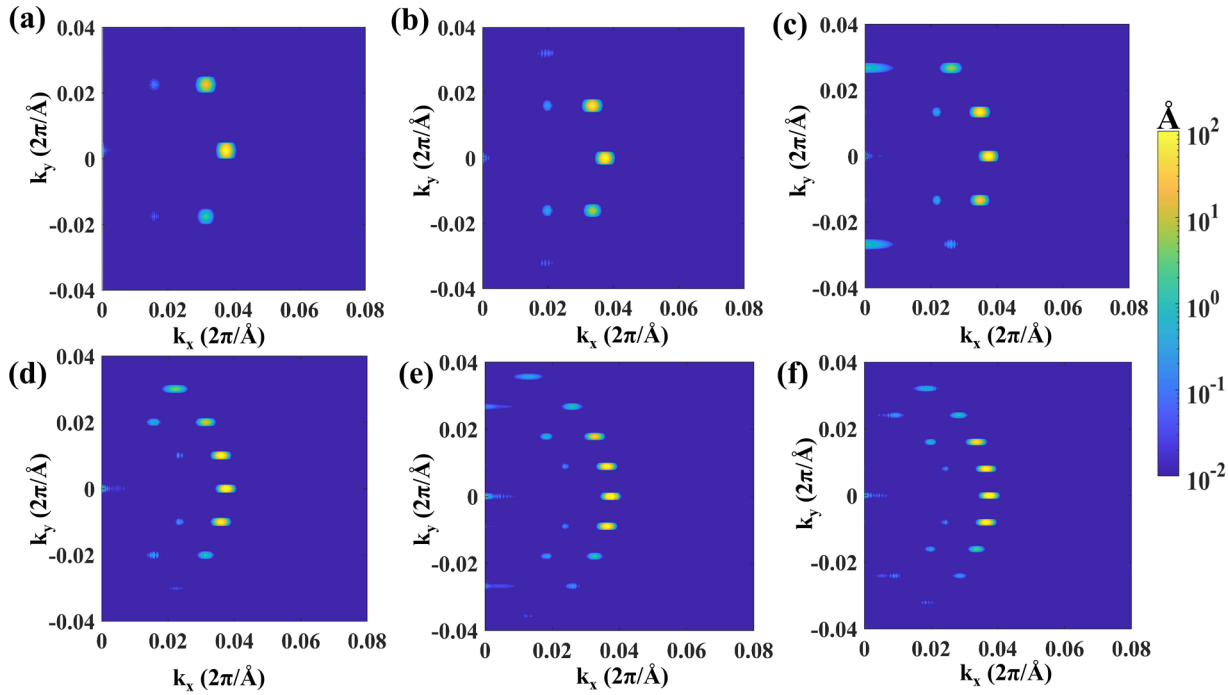

FIG. 8. The 2D FFT of u_y after the phonon wave passes through the metagrating structure with different widths D_y. (a) $D_y = 49.8$ Å; (b) $D_y = 62.3$ Å; (c) $D_y = 74.8$ Å; (d) $D_y = 87.2$ Å; (e) $D_y = 99.7$ Å; and (f) $D_y = 112.1$ Å. The side-bar color coding represents the amplitude of the FFT results $B_{j\alpha}(\mathbf{k})$ for the transmitted modes in the unit of Å. Here, $D_x = 550$ Å is used in the simulations, and the TA mode with $k_0 = 0.0373$ $(2\pi/\text{Å})$ is used as the normally incident wave packet.

[1] N. Yu, P. Genevet, M. A. Kats, F. Aieta, J. P. Tetienne, F. Capasso, and Z. Gaburro, Science **334**, 333 (2011).

[2] J. Hao, Y. Yuan, L. Ran, T. Jiang, J. A. Kong, C. T. Chan, and L. Zhou, Phys. Rev. Lett. **99**, 063908 (2007).

[3] L. Li, T. Li, X.-M. Tang, S.-M. Wang, Q.-J. Wang, and S.-N. Zhu, Light Sci. Appl. **4**, e330 (2015).

[4] X. Ni, N. K. Emani, A. V. Kildishev, A. Boltasseva, and V. M. Shalaev, Science **335**, 427 (2012).

[5] S. Sun, K. Y. Yang, C. M. Wang, T. K. Juan, W. T. Chen, C. Y. Liao, Q. He, S. Xiao, W. T. Kung, G. Y. Guo *et al.*, Nano Lett. **12**, 6223 (2012).

[6] J. Hao, J. Wang, X. Liu, W. J. Padilla, L. Zhou, and M. Qiu, Appl. Phys. Lett. **96**, 251104 (2010).

[7] N. Liu, M. Mesch, T. Weiss, M. Hentschel, and H. Giessen, Nano Lett. **10**, 2342 (2010).

[8] S. Sun, Q. He, S. Xiao, Q. Xu, X. Li, and L. Zhou, Nat. Mater. **11**, 426 (2012).

[9] L. Huang, X. Chen, B. Bai, Q. Tan, G. Jin, T. Zentgraf, and S. Zhang, Light Sci. Appl. **2**, e70 (2013).

[10] F. Aieta, P. Genevet, M. A. Kats, N. Yu, R. Blanchard, Z. Gaburro, and F. Capasso, Nano Lett. **12**, 4932 (2012).

[11] X. Chen, L. Huang, H. Muhlenbernd, G. Li, B. Bai, Q. Tan, G. Jin, C. W. Qiu, S. Zhang, and T. Zentgraf, Nat. Commun. **3**, 1198 (2012).

[12] N. L. Tsitsas and C. Valagiannopoulos, Phys. Rev. Res. **2**, 033526 (2020).

[13] M. Rahmanzadeh and A. Khavasi, Opt. Express **28**, 16439 (2020).

[14] Y. Li, X. Jiang, R. Q. Li, B. Liang, X. Y. Zou, L. L. Yin, and J. C. Cheng, Phys. Rev. Appl. **2**, 064002 (2014).

[15] Y. Li, C. Shen, Y. Xie, J. Li, W. Wang, S. A. Cummer, and Y. Jing, Phys. Rev. Lett. **119**, 035501 (2017).

[16] K. Tang, C. Qiu, M. Ke, J. Lu, Y. Ye, and Z. Liu, Sci. Rep. **4**, 6517 (2014).

[17] Y. F. Zhu, X. Y. Zou, R. Q. Li, X. Jiang, J. Tu, B. Liang, and J. C. Cheng, Sci. Rep. **5**, 10966 (2015).

[18] Y. Li and M. B. Assouar, Sci. Rep. **5**, 17612 (2015).

[19] S. Qi, Y. Li, and B. Assouar, Phys. Rev. Appl. **7**, 054006 (2017).

[20] J. Chen, X. Xu, J. Zhou, and B. Li, Rev. Mod. Phys. **94**, 025002 (2022).

[21] J. Chen, J. He, D. Pan, X. Wang, N. Yang, J. Zhu, S. A. Yang, and G. Zhang, Sci. China Phys. Mech. Astron. **65**, 117002 (2022).

[22] R. A. Guyer and J. A. Krumhansl, Phys. Rev. **148**, 778 (1966).

[23] A. J. Minnich, J. Phys.: Condens. Matter **27**, 053202 (2015).

[24] W. Ren, J. Chen, and G. Zhang, Appl. Phys. Lett. **121**, 140501 (2022).

[25] H. Wang, H. Hu, N. Man, C. Xiong, Y. Xiao, X. Tan, G. Liu, and J. Jiang, Mater. Today Phys. **16**, 100298 (2021).

[26] X. Peng, P. Jiang, Y. Ouyang, S. Lu, W. Ren, and J. Chen, Nanotechnology **33**, 035707 (2021).

[27] Z. Zhang, S. Hu, J. Chen, and B. Li, Nanotechnology **28**, 225704 (2017).

[28] W. Ren, S. Lu, C. Yu, J. He, Z. Zhang, J. Chen, and G. Zhang, Appl. Phys. Rev. **10**, 041404 (2023).
[29] M. N. Luckyanova, J. Garg, K. Esfarjani, A. Jandl, M. T. Bulsara, A. J. Schmidt, A. J. Minnich, S. Chen, M. S. Dresselhaus, Z. Ren *et al.*, Science **338**, 936 (2012).
[30] M. Simoncelli, N. Marzari, and F. Mauri, Nat. Phys. **15**, 809 (2019).
[31] L. Isaeva, G. Barbalinardo, D. Donadio, and S. Baroni, Nat. Commun. **10**, 3853 (2019).
[32] P. Jiang, Y. Ouyang, W. Ren, C. Yu, J. He, and J. Chen, APL Mater., **9**, 040703 (2021).
[33] Z. Zhang, Y. Guo, M. Bescond, J. Chen, M. Nomura, and S. Volz, Phys. Rev. Lett. **128**, 015901 (2022).
[34] Y. Guo, Z. Zhang, M. Bescond, S. Xiong, M. Nomura, and S. Volz, Phys. Rev. B **103**, 174306 (2021).
[35] N. Yu and F. Capasso, Nat. Mater. **13**, 139 (2014).
[36] Q. Zheng *et al.*, Sci. Adv. **7**, eabg0363 (2021).
[37] C. Jung, G. Kim, M. Jeong, J. Jang, Z. Dong, T. Badloe, J. K. W. Yang, and J. Rho, Chem. Rev. **121**, 13013 (2021).
[38] H. Qiao *et al.*, Science **380**, 1030 (2023).
[39] G. S. MacCabe, H. Ren, J. Luo, J. D. Cohen, H. Zhou, A. Sipahigil, M. Mirhosseini, and O. Painter, Science **370**, 840 (2020).
[40] D. Zhu *et al.*, Nano Lett. **17**, 915 (2017).
[41] F. R. Braakman, N. Rossi, G. Tutuncuoglu, A. F. I. Morral, and M. Poggio, Phys. Rev. Appl. **9**, 054045 (2018).
[42] P. K. Schelling, S. R. Phillpot, and P. Keblinski, Appl. Phys. Lett. **80**, 2484 (2002).
[43] S. Hu, Z. Zhang, P. Jiang, J. Chen, S. Volz, M. Nomura, and B. Li, J. Phys. Chem. Lett. **9**, 3959 (2018).
[44] S. Plimpton, J. Comput. Phys. **117**, 1 (1995).
[45] L. Lindsay and D. A. Broido, Phys. Rev. B **81**, 205441 (2010).
[46] C. A. Valagiannopoulos, Prog. Electromagn. Res. C **3**, 203 (2008).
[47] A. B. Shvartsburg, S. Jiménez, N. S. Erokhin, and L. Vázquez, Phys. Rev. Appl. **11**, 044056 (2019).
[48] T. Feng, Y. Zhong, J. Shi, and X. Ruan, Phys. Rev. B **99**, 045301 (2019).
[49] Y. Xie, W. Wang, H. Chen, A. Konneker, B. I. Popa, and S. A. Cummer, Nat. Commun. **5**, 5553 (2014).
[50] Y. Li, X. Jiang, B. Liang, J.-C. Cheng, and L. Zhang, Phys. Rev. Appl. **4**, 024003 (2015).
[51] S. Tamura, D. C. Hurley, and J. P. Wolfe, Phys. Rev. B **38**, 1427 (1988).
[52] T. Yoshihiro and N. Nishiguchi, Phys. Rev. B **100**, 235441 (2019).
[53] B. Assouar, B. Liang, Y. Wu, Y. Li, J.-C. Cheng, and Y. Jing, Nat. Rev. Mater. **3**, 460 (2018).
[54] S. Zhang, Y. Zhang, Y. Guo, Y. Leng, W. Feng, and W. Cao, Phys. Rev. Appl. **5**, 034006 (2016).
[55] N. Mohammadi Estakhri and A. Alù, Phys. Rev. X **6**, 041008 (2016).
[56] J. Mahmood *et al.*, Nat. Commun. **6**, 6486 (2015).
[57] C. Moreno *et al.*, Science **360**, 199 (2018).
[58] J. Ravichandran *et al.*, Nat. Mater. **13**, 168 (2014).
[59] Y.-X. Yan, E. B. Gamble, and K. A. Nelson, J. Chem. Phys. **83**, 5391 (1985).
[60] F. Glerean, S. Marcantoni, G. Sparapassi, A. Blason, M. Esposito, F. Benatti, and D. Fausti, J. Phys. B: At. Mol. Opt. Phys. **52**, 145502 (2019).
[61] H. S. Casalongue, S. Kaya, V. Viswanathan, D. J. Miller, D. Friebel, H. A. Hansen, J. K. Nørskov, A. Nilsson, and H. Ogasawara, Nat. Commun. **4**, 2817 (2013).
[62] M. Hase, K. Mizoguchi, H. Harima, S. Nakashima, M. Tani, K. Sakai, and M. Hangyo, Appl. Phys. Lett. **69**, 2474 (1996).
[63] M. Farhat, S. Guenneau, and H. Bagci, Phys. Rev. Lett. **111**, 237404 (2013).
[64] J. Schiefele, J. Pedros, F. Sols, F. Calle, and F. Guinea, Phys. Rev. Lett. **111**, 237405 (2013).
[65] Y. Luo, A. Martin-Jimenez, M. Pisarra, F. Martin, M. Garg, and K. Kern, Nat. Commun. **14**, 3484 (2023).